Anisotropic fracture in nacre-like alumina

Thomas Duminy, Ronan Henry, Jérôme Adrien, Aurélien Doitrand, Sylvain Meille

Anisotropic fracture in nacre-like alumina

Thomas Duminy[✉a], Ronan Henry[a,1], Jérôme Adrien[a], Aurélien Doitrand[a], Sylvain Meille[a]

[a] *Univ Lyon, INSA Lyon, UCBL, MATEIS UMR CNRS 5510, Villeurbanne, F-69621, France*
e-mail: thomas.duminy@insa-lyon.fr
postal address: 345 Avenue Gaston Berger, 69100 Villeurbanne, FRANCE

Abstract

Fracture in nacre-like alumina is studied experimentally and numerically with alumina platelets main alignment direction perpendicular (along-configuration) to the one commonly tested (across-configuration) in the literature. In along-configuration, brittle failure is noted after crack initiation with no macroscopic crack deviation, unlike what is observed in across-configuration. However, NLA exhibits in along configuration initiation critical stress intensity factor $K_{Ic} = 5.3 \pm 0.5$ MPa.m$^{1/2}$, in the same order of magnitude as in across-configuration. The increase in K_{Ic} compared to monolithic alumina can be explained by a phenomenon of crack initiation containment at the interface between platelets. Unstable crack propagation occurs just after initiation, mainly following the platelet interfaces which results in crenelated fracture surfaces with crack decentering with respect to the initial notch tip.

Keywords: Finite fracture mechanics, nacre-like alumina, crack initiation, anisotropy

1. Introduction

Ceramics usually show limited fracture toughness associated with a brittle behavior at ambient temperature, which is a severe limitation to a wider use as structural materials. Increasing crack resistance of ceramics has therefore been a major theme of research, mainly by the development of extrinsic mechanisms, *i.e.* mechanisms that act behind the crack tip, to hinder crack propagation [1]. Some examples of extrinsic mechanisms in ceramic materials are phase transformation [2] [3], crack bridging [4] or crack deflection [5] [6]. Nacre has been studied for more than thirty years [7] [8] as it exhibits a toughness three orders of magnitude higher than the one of its constituents [9].

[1] Now at Normandie Univ, UNIV ROUEN, INSA Rouen, CNRS, Groupe de Physique des Matériaux, Rouen, 76000, France

Natural nacre is composed of 95 vol.% of staggered stiff calcium carbonate platelets ($CaCO_3$) embedded in 5 vol.% of a compliant secondary phase made of proteins [8] [10]. Consequently, its structure is often referred to as 'brick-and-mortar' by analogy with masonry. Toughening in nacre is explained by several extrinsic mechanisms that act at different length scales, namely breaking of mineral bridges that form between platelets [11], interlocking of platelets [12] [13], platelet pull-out, and crack deflection in the secondary phase [13] [14] [15] [16].

Efforts have been made in the last two decades to manufacture artificial nacres that replicate the brick-and-mortar microstructure of natural nacre. Such materials consist of micron-sized ceramic platelets embedded in a secondary phase. The platelets are generally made of mono-crystalline alumina [17] [18] [19] while the secondary phase can be for instance a metal [20] or a polymer [21] [22]. To avoid the decrease in fracture strength associated with the use of ductile secondary phases and to envision using these materials at elevated temperatures, full mineral solutions have been developed [17] [23]. Recent works focused on the manufacturing and on the mechanical characterization of nacre-like alumina (NLA), made of alumina platelets embedded in an amorphous glassy phase [24] [25] [26]. This configuration results in a material having, along across direction, a strength typical of dense polycrystalline alumina (430 $\pm$ 30 MPa), but with a crack initiation stress intensity factor more than twice higher (5.8 $\pm$ 0.2 MPa.m$^{1/2}$). Using a mineral secondary phase thus leads to a trade-off between toughness and strength for a ceramic material [26].

Heretofore the knowledge of the mechanical properties of NLA remains fragmentary, especially when considering the anisotropic character of NLA. Indeed, resistance to crack propagation in these materials has almost exclusively been characterized using Single Edge Notched Beam (SENB) in bending in a configuration resulting in extensive crack deflection at the interfaces between platelets, *i.e.* with alumina platelet *c-axis* being mainly collinear with the SENB height (*x-axis*) (both axes are defined on Fig. 1) [17] [18] [27]. This configuration is referred to as *across*-configuration [28] in this paper (Fig. 1 - Top Left). Some attempts have been made to characterize the anisotropy of mechanical properties in nacre-like materials, but they were mostly limited to compressive tests on nacre-like with ductile secondary phase [29] [30]. Chan *et al.* [30] infiltrated alumina platelet scaffolds with different platelet orientations with polydimethylsiloxane. They show that stiffness,

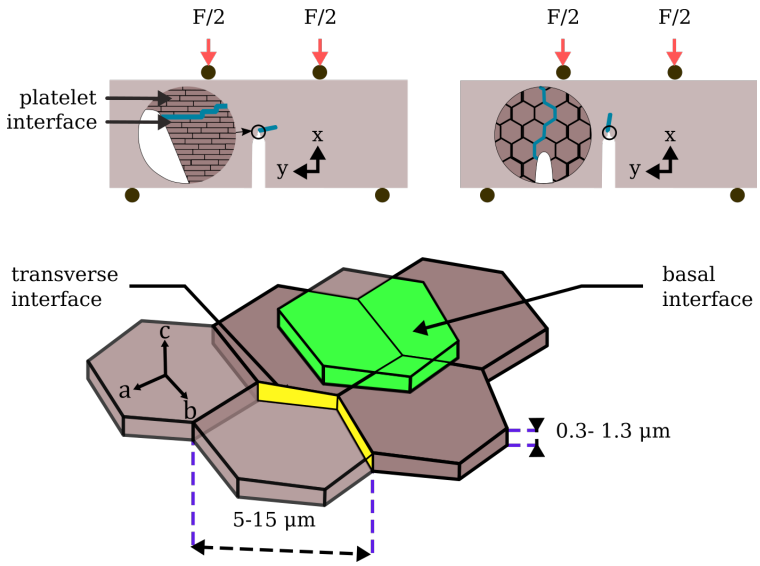

Figure 1: (Top): Schematic representation of a NLA SENB sample with platelets in (Left) *across*-configuration, (Right) *along*-configuration. The crack is schematized by the blue lines. (Bottom) Schematic representation of platelet local arrangement. Two kinds of interfaces can be depicted: green interfaces are labelled as *basal interfaces* and yellow interfaces are labelled as *transverse interfaces*.

strength and toughness vary with the platelet orientation with respect to the loading direction. Akurati *et al.* [29] tested NLA with epoxy as a secondary phase. They show that different deformation mechanisms can be triggered depending on the platelet orientation. In addition, indentation tests on NLA with alumina platelet and amorphous glassy phase were performed to characterize the anisotropy of the material [31]. Both anisotropy in Young's modulus and hardness where assessed for temperature ranging from room temperature to 550°C. All of these studies were focused on NLA in *across*-configuration (see Fig 1 - Top Left). However, none of these studies investigated the behaviour of NLA with the platelet *c-axis* being collinear with the sample *z-axis* (*i.e.* obtained by 90° rotation from *across*-configuration around the *y-axis* as illustrated in Fig. 1 - Top Right and hereafter referred to as *along*-configuration [28]).

Understanding and characterizing fracture mechanisms for other material orientations than 'across configuration' appears crucial to envision using NLA as structural materials. The objective of this work is therefore to characterize crack initiation and propagation in NLA in another platelet orientation than the commonly studied one. The experimental characterization of NLA in *along*-

configuration both at macro- and micro-scale is presented in Section 2. Section 3 is dedicated to the modelling of crack initiation using the coupled criterion at both scales, a comparison with experiments is then provided in section 3.3. The results are finally discussed and compared to those obtained in *across*-configuration.

2. Experimental characterization of NLA: along-configuration

2.1. Methods

2.1.1. Mechanical testing at the macro-scale

4-points bending tests (4PB) are carried out on SENB samples. The composition of these samples is the same as in [17] [24] [25], namely 95.0 vol% of α-Al_2O_3 monocrystalline platelets and 5.0 vol% of glass phase (SiO_2-Al_2O_3-CaO (65:25:10 wt.%)). The manufacturing process is the same as in [24], *i.e.* field assisted sintering of a freeze-dried powder. This results in a material relative density after sintering of 98% (3.88 g.cm^{-3}) [24]. Mechanical characterization being the main standpoint of the present article, the reader is referred to the previously cited articles for further details on the manufacturing process.

Macroscopic bending tests were carried out using a uniaxial testing machine (Instron 8562, High Wycombe UK) with support span distance of 12 mm and a loading span distance of 3 mm (Fig. 1 - Top Right). Critical stress intensity factors K_{Ic} values are computed according to [32].

Geometrical parameters of tested samples are illustrated in Fig. 2 and listed in Table 1. A diamond-saw notch of approximately 200 μm width and 1.9 mm depth refined by a razor blade is machined in each sample to act as crack promoter. The notch tip radius lies between 5 and 8 μm depending on the sample (see Table 1).

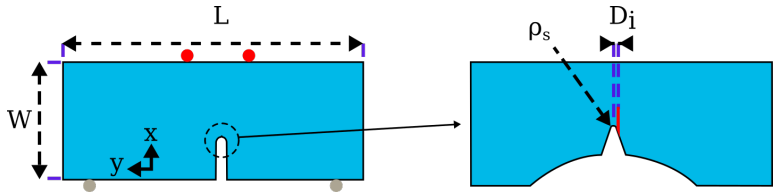

Figure 2: Schematic representation of the samples and definition of geometrical parameters. Left: general view of the specimen. Right: magnification of the notch tip. The crack is schematized in red. The dimension of the sample along the *z-axis* (thickness) is depicted by the parameter B in Table 1.

Sample	L (mm)	W (mm)	B (mm)	ρ_s (μm)	F_{init}^{exp} (N)
S_1	14.9	5.3	1.9	8.0	224
S_2	14.8	5.3	1.9	5.7	231
S_3	15.1	4.9	2.0	5.0	273
S_4	15.4	5.0	2.0	5.1	221

Table 1: Samples geometrical dimensions, notch tip radius and experimental force at crack initiation F_{init}^{exp}.

2.1.2. Imaging technique characterization

Fracture surfaces of tested samples are characterized by different imaging techniques to identify the failure mechanisms. Scanning Electron Microscopy (SEM) observations are assessed to evaluate the interaction of the crack with the microstructure of gold sputter coated samples. Gold coating is applied on the surface of the samples to avoid charging effect, *i.e.* accumulation of electrons at the surface of the sample that would dramatically affect the observation quality. They are conducted on a VEGA 3 SEM (Tescan, Brno, Czech Republic) under an accelerating voltage of 10kV and using secondary electrons. SEM allow for high quality observation but are rather limited to acquire out-of-plane quantitative information. Micro-computed tomography (μ-CT) is performed with a 2 μm voxel size using an EasyTom Nano tomography system (RX Solutions, Annecy, France). The principle is the following. The sample under investigation is mounted on a rotor. An X-ray beam is sent on the sample. 650 scans are acquired, each of them taken at a different angular position of the sample. The transmitted X-ray beam signal is acquired by a charge coupled device camera. Then, a reconstruction software gathers all scans to obtain a three dimensional-distribution of the linear X-ray attenuation coefficient within the sample. This 3D distribution forms an image from which one can extract 2D sections (see Fig. 6 - Left). The distribution of X-ray attenuation can be related to a density variation, thus allowing for the identification of cracks inside a sample, providing their dimensions are larger than the spatial resolution, i.e. approximately 2 to 3 times the voxel size. With the set-up used, the major cracks could be identified. However, the interaction between a crack and its neighbouring platelets cannot be assessed as the platelet characteristic dimensions are below the μ-CT resolution.

Therefore, confocal observations of the fracture surface are carried out using an NPS-NP1 con-

focal sensor (Hirox, Tokyo, Japan) with a lateral resolution of 1 μm and a height resolution of 20 nm. Confocal microscopy allows for a 3-dimensional topological reconstruction of the surface and for height profile measurement, only a fraction of the total fracture surface being observed to limit the acquisition time at such high resolution. This surface reconstruction first enables to determine the exact location of the notch tip as the junction between the razor-blade machined notch and the crack surface. Then, 2-dimensional profiles are measured on the crack surface close to the notch tip corresponding to the crack initiation site.

2.1.3. Bending tests on micro-cantilever beams

In addition to macroscale four-points bending tests, we also analyse a micro-cantilever test carried out on NLA in *along*-configuration on samples processed using the same manufacturing route as in [24] [25], resulting in similar composition and microstructure. The sample was prepared using a Focalized Ion Beam (FIB) (NVision 40, Carl Zeiss, Oberkochen, Germany) with gallium ions at an accelerating voltage of 30 kV. Ionic currents from 3 nA down to 300 pA were used for the milling steps [25]. The obtained micro-cantilever has a pentagonal section. The force was applied *ex situ* using a nano-indenter under displacement control (G200, Keysight, Santa Rosa, USA). Fig. 3 - Left is a schematic representation of the micro-cantilever beam before testing.

Figure 3: (Left): Schematic of a micro-cantilever sample in *along*-configuration prepared by FIB. Some platelets are illustrated in brown. The black arrow indicates the loading location. (Middle): Micro-cantilever fracture surface after testing in *along*-configuration. (Right): Definition of geometric features and of the possible crack initiation sites. The corresponding color code will be explained in Section 3

2.2. Results

2.2.1. 4-points bending tests

The force-displacement curves of the macroscopic NLA samples tested in *along*-configuration are shown in Fig. 5. All samples exhibit an elastic brittle behavior. No stable crack propagation was observed. The crack path observed on the specimen surface seems at first sight similar to that of a homogeneous isotropic material - crack propagating parallel to the notch direction (see Fig. 4). The forces at crack initiation are listed in Table 1. Critical stress intensity factor at

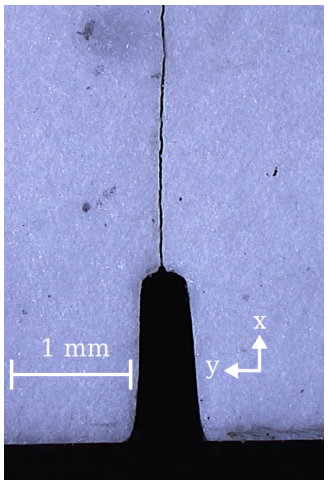

Figure 4: Macroscopic observation of the crack propagation direction on a sample tested in four-points bending.

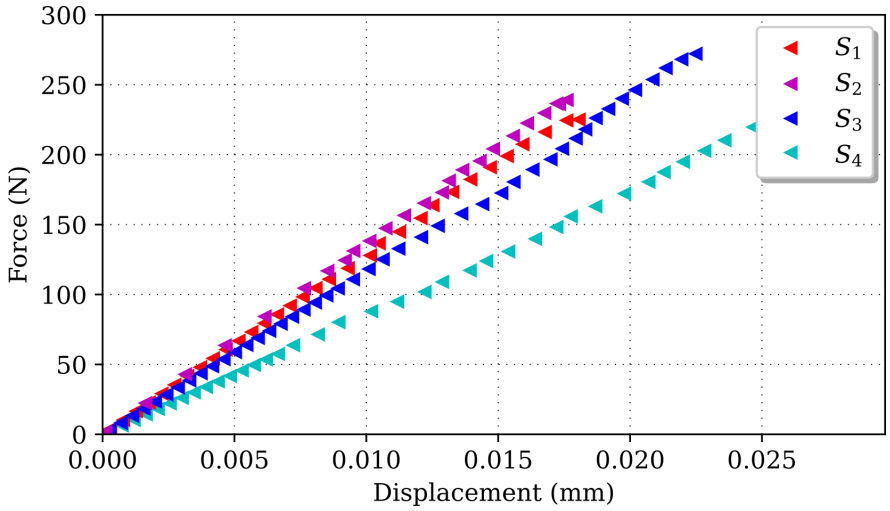

Figure 5: Force-displacement curves of NLA samples tested in 4-points bending in *along*-configuration.

initiation (K_{Ic}) values were computed for each specimen, resulting in $K_{Ic} = 5.3 \pm 0.5$ MPa.m$^{0.5}$.

In *across*-configuration on samples of the same composition and process conditions, Saad *et al.* obtained an apparent critical stress intensity factor at initiation equal to 5.8 ± 0.2 MPa.m$^{0.5}$ [24].

2.2.2. Micro-computed tomography

Fig. 6 - Left shows four tomography slices selected at different locations along the thickness of a beam tested in 4-points bending, as illustrated in Fig. 6 - Right. We observe that the crack is not always centered with respect to the notch bisector, resulting in some crack decentering as illustrated by the parameter D_i (Fig 2 - Right). This decentering is not constant for one sample, but varies across the sample thickness (along the *z-axis* direction) (see Fig. 3). D_i values at different locations along the thickness cannot be accurately determined from the μ-CT data since the spatial resolution is not sufficient.

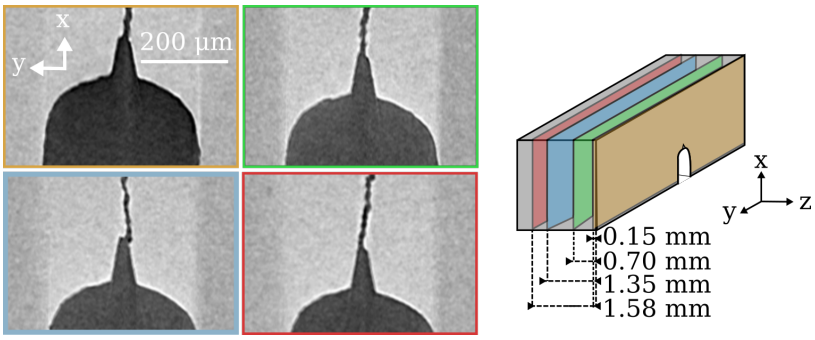

Figure 6: μ-CT slices at different locations along the thickness of a NLA sample tested in 4-points bending, showing the deviation of the crack location with respect to the notch plane. The image on the right gives the distance of each μ-CT observation from the sample side.

2.2.3. SEM observations

The fracture surface roughness is evidenced in Fig. 7, which can be explained by cracking mainly occurring along the interfaces between the platelets. Platelet misalignment with respect to their main orientation direction is also observed, as already characterized by Saad *et al.*, *i.e.* 15° mean platelet misalignment with respect to the plane perpendicular to the pressing direction during processing. Only two broken platelets are observed as shown inside white ellipses. Broken platelets can be identified by the presence of spherical pores on the fractured surface (corresponding to initially close porosity inside the platelets). Indeed, porosity is not observed on the surface of unbroken platelet [25] [33].

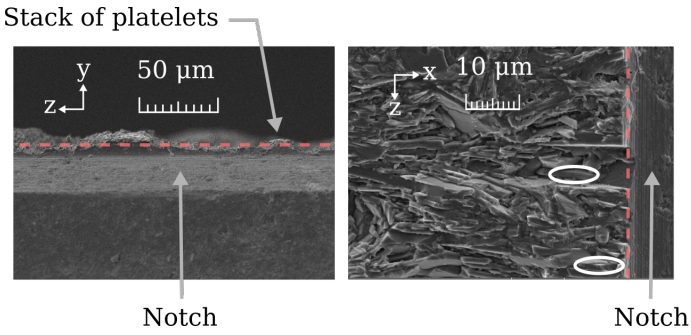

Figure 7: (Left): SEM image (bottom view) of a SENB sample after bending test showing interactions of the crack with the microstructure. The razor blade notch lies in the foreground and the crack surface in the background. (Right): SEM image view of a SENB sample after test showing the presence of two broken platelets (as shown with white ellipses). The axis systems are defined in accordance with Fig. 1. On both images, the red dashed lines depict the notch tip.

2.2.4. Confocal microscopy

As confocal microscopy has a better spatial resolution as compared to X-ray tomography, it enables the quantification of surface roughness. Fig 8 shows a 3D reconstructed fracture surface near the notch tip, evidencing the fracture surface roughness due to crack propagation along the interface between platelets. A 2D profile is captured at the junction between the notch and the

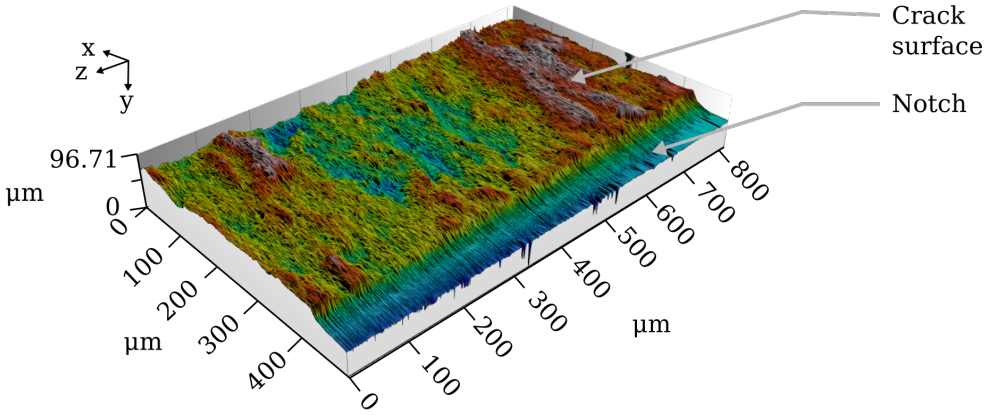

Figure 8: Partial confocal reconstruction of a SENB sample fracture surface.

fracture surface along the *z-axis*. It corresponds to the evolution of D_i along the SENB thickness. The profile is shown in Fig. 9. The arithmetical mean deviation of the profile equals 6.5 μm and the maximum height variation of the profile equals 46.5 μm [34].

It can be concluded from the different imaging technique results (SEM, XRay tomography,

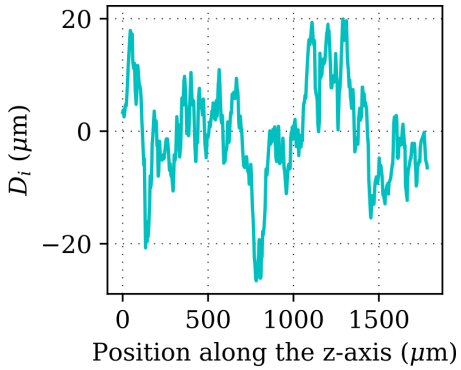

Figure 9: D_i evolution as a function of the position along the sample thickness.

profilometry) that crack initiates along the interface between platelets, with local deviations around platelets. However, no macroscopic crack deviation is observed (see Fig. 4) which is a major difference with NLA tests in *across*-configuration where a crack deviation of typically 70° to 80° from the notch plane can be observed at the macroscopic scale [35]. Two hypotheses on the crack initiation location in *along*-configuration can thus be proposed:

- The crack initiates on a *transverse interface* at the scale of one platelet - *i.e.* approximately 0.5 μm in the *z-direction* (see the corresponding yellow interface in Fig. 1).
- The crack initiates on a *basal interface* with a larger surface (see the corresponding green interface in Fig. 1-bottom).

2.2.5. Bending test on microcantilever

We observed a linear elastic behavior up to brittle fracture. The force at crack initiation is 3.0 mN. The microcantilever tested in bending as shown in Fig. 3 exhibits a non-flat fracture surface, with crenellations of one to four platelets thick. As compared to the macro-scale tests, the fraction of broken platelets in the fracture surface is larger at the microscale (see surfaces showing small spherical pores in Fig. 3). However, these pores are mainly located on the beam area loaded under compression. Therefore, this may indicate that crack initiation occurs at the interface between platelets and subsequent unstable crack propagation causes platelets fracture. Fig. 3 - Middle shows that 4 interfaces are possible crack initiation interfaces. They are shown on Fig. 3 - Right.

3. Simulation

3.1. Methods

3.1.1. The coupled criterion

The coupled criterion (CC) is a method developed by *Leguillon* [36] for the prediction of crack initiation. It states that the stress must be larger than the tensile strength over the whole area corresponding to the crack before initiation, and that the potential energy released by crack initiation must be larger than the energy required for the creation of the crack surfaces. These conditions write:

$$\begin{cases} \sigma_{nn} & \geq \sigma_c \\ -\Delta W & \geq \mathcal{G}_{\mathrm{c}} \Delta S \end{cases} \tag{1}$$

with σ_{nn} the opening stress along the path of the newly created crack before initiation, σ_c the tensile strength, ΔW the potential energy variation due to crack opening, ΔS the crack surface, and $\mathcal{G}_{\mathrm{c}}$ the material critical energy release rate.

This can also be written as:

$$\begin{cases} \sigma_{nn} & \geq \sigma_c, \\ -\frac{\Delta W}{\Delta S} = \mathcal{G}_{inc} & \geq \mathcal{G}_{\mathrm{c}}, \end{cases} \tag{2}$$

where $\mathcal{G}_{inc}$ is the incremental energy release rate.

Both conditions can be normalized:

$$\begin{cases} \frac{\sigma_{nn}}{\sigma_c} & \geq 1, \\ \frac{\mathcal{G}_{\mathrm{inc}}}{\mathcal{G}_c} & \geq 1. \end{cases} \tag{3}$$

Since the stress criterion is generally a decreasing function of the crack surface, it provides an upper bound for the admissible range of crack initiation surface S_c. On the contrary the energy criterion is generally an increasing function of the crack surface [37]. Consequently, it yields a lower bound for the admissible initiation crack surface range. For a too small imposed loading, the upper bound obtained with the stress criterion is smaller than the lower bound obtained with the energy criterion, which means there is no crack surface for which both criteria are fulfilled (Fig. 10). Therefore, loading must be increased in order to increase the upper bound given by the stress criterion while decreasing the lower bound given by the energy criterion until both bounds

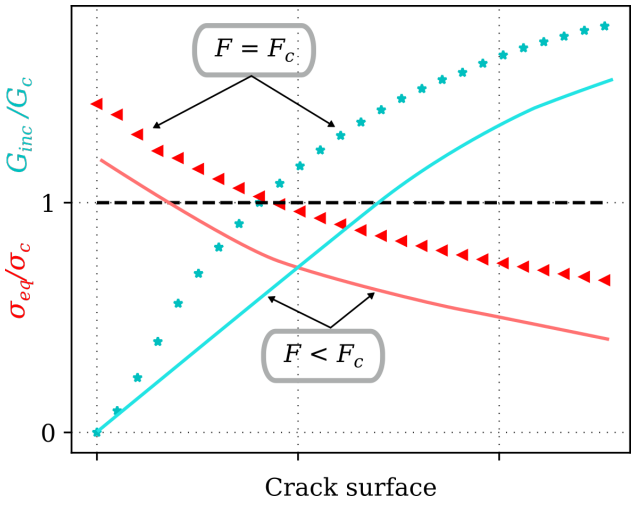

Figure 10: Schematic explanation of the CC: energy (light blue) and stress criteria (red) as a function of crack surface for imposed loadings equal to (dotted lines) or lower (full lines) than the crack initiation loading.

match, which enables determining the imposed loading at crack initiation. As a consequence, the criterion induces that a crack can only initiate for a finite length, contrary to infinitesimal crack extensions obtained in LEFM [38]. It is worth noting that in the particular case of a pre-existing crack under displacement control, the coupled criterion is consistent with LEFM as it also admits infinitesimal crack propagation [39] [40].

The above explanation is schematically illustrated in Fig. 10, the two criteria from (3) being plotted as a function of the crack surface for two different loadings.

When the applied loading is high enough (*i.e.* $F = F_c$, dotted lines on Fig. 10), for crack surfaces smaller than the one corresponding to the intersection of both curves, the stress criterion is fulfilled but not enough energy would be released by the creation of such cracks. On the contrary, a too large crack cannot initiate since the stress criterion would not be fulfilled on the whole crack path before initiation. The intersection of the two curves represents the crack surface for which the two criteria are fulfilled simultaneously.

NLA exhibits linear elastic behavior before crack initiation. Consequently, under the hypothesis of small deformations, the proportionality between stress and applied displacement U_0 and between potential energy and square of applied displacement writes:

$$\begin{cases} \sigma_{nn}(S) = k(S)U_0 & \geq \sigma_c, \\ \mathcal{G}_{inc}(S) = A(S)U_0^2 & \geq \mathcal{G}_{inc}, \end{cases} \tag{4}$$

With $k(S)$ and $A(S)$ the two proportionality functions.

The aim is thus to find, among all possible value for the applied displacement U, a critical displacement U_c, which corresponds to the smallest imposed displacement that fulfils both conditions of the CC:

$$\begin{cases} U(S) = \max(\sqrt{\frac{\mathcal{G}_{inc}}{A(S)}}; \frac{\sigma_c}{k(S)}), \\ U_c = \min_S(U(S)). \end{cases} \tag{5}$$

As can been seen from all equations above, determining U_c requires the knowledge of the stress field - and thus the function k - and of the potential energy released as a function of the crack length - and thus the function A. Then, the predicted initiation force is derived from the obtained value of the critical displacement and can be compared to forces measured experimentally. The stress and potential energy are obtained by FE calculations as explained in next section. Functions A and k depend on the crack geometry. Assuming a given crack geometry, U_c can be determined using the above-mentioned method. If the crack path is unknown, it may be determined as the one minimizing U_c among all possible cracks, which may be computationally costly. In the sequel, the possible crack configurations are based on experimental observations.

3.1.2. 2D implementation of the coupled criterion at the macroscale

A 2D model of SENB sample is shown in Fig. 2. The numerical sample dimensions are set to the mean values of the 4 tested samples. NLA displays a transversely isotropic behavior at the macroscopic scale and its elastic properties have been determined using ultrasonic contact technique. The shear and longitudinal wave speeds in the material are directly related to E and ν and are calculated using a transmitter/receiver sensor working at a frequency of 5 MHz. We obtained $E_{aa} = E_{bb} = 368$ GPa Young's modulus in the direction of the platelet plane, $E_{cc} = 320$ GPa Young's modulus in the transverse direction (along platelet *c-axis*), $\nu_{ab} = 0.24$ and $\nu_{ac} = 0.24$ Poisson's ratio in the platelet plane and transverse direction respectively [35].

In Fig. 2-Left, the red circles indicate a vertical imposed displacement along the *x-axis* and the

grey circles indicate a vertical displacement set to 0.0 mm along the *x-axis* to model the fixed spans. Quadratic triangular elements are chosen with a minimum mesh size of 0.2 μm around the crack, whose path is modelled as a segment. Such a configuration results in about 7 000 degrees of freedom. Mesh convergence is ensured so that initiation force differences smaller than 1% are obtained when using a finer mesh discretization.

From Section 3.1.1, we know that solving the CC requires the knowledge of the functions *k(S)* and *A(S)* defined in Eq 4. The function *k(S)*, which links the imposed displacement and the stress field, is obtained based on FE simulation without crack. Then, the nodes along the crack path are successively released. For each crack surface, the elastic strain energy is computed which enables calculating the function *A(S)*.

Crack initiation and propagation in NLA in *across*-configuration is an interfacial process [17] [25]. Doitrand *et al.* [35] determined NLA interface tensile strength σ_c and critical energy release rate $\mathcal{G}_c$ for *across*-configuration from macro- and micro-scale bending tests. Additionally, strength and toughness for a single alumina platelet was determined in [41] from microbending tests [33]. These material parameters are listed in Table 2.

	Strength (MPa)	**Toughness** (J.m^{-2})
Al_2O_3 platelets [41]	1100	22
Interface [35]	438	1.9

Table 2: Fracture parameters used in the 2D model.

3.1.3. 3D implementation of the coupled criterion at the macroscale

Fig. 11 shows a schematic illustration of the SENB 3D model. The upper cylinders illustrate the roller location where displacement is imposed along the *x-axis*. The lower cylinders depict the support location. Quadratic tetrahedron are used, with a 0.1 μm minimum mesh size around the crack. This model contains about 700 000 degrees of freedom. The same mesh convergence procedure than in Section 3.1.2 is applied.

Adding a third dimension to the model enables modelling a planar crack of finite thickness. The crack is always assumed to initiate at mid-thickness of the crack plane. The possible crack shapes are determined after a first FE simulation by assuming they coincide with the stress isocontours,

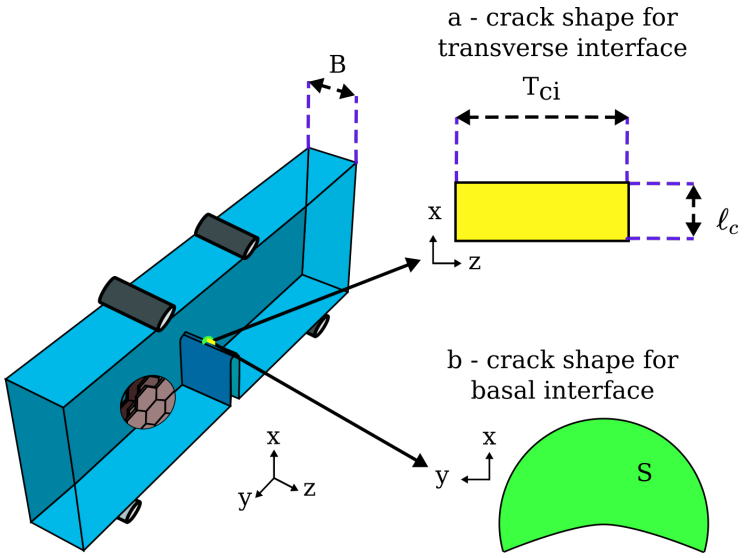

Figure 11: Macroscopic 3-dimensional model. The material is considered homogeneous. A magnification of the microstructure is represented on the front-left part of the sample. The yellow rectangle represents the crack shape at initiation under transverse interface assumption. The green circular shape represents the crack shape at initiation under basal interface assumption.

as proposed by Doitrand and Leguillon [42] [43]. The same elastic and fracture parameters as in the 2D model are used. Since experimental observations lead to assumption of crack initiation either at the *basal* or *transverse interfaces*, these two hypotheses can be tested. Fig. 12 shows a schematic representation of some platelets in *along*-configuration with some interfaces between platelets represented in green and yellow for the *basal* - and *transverse interfaces* respectively.

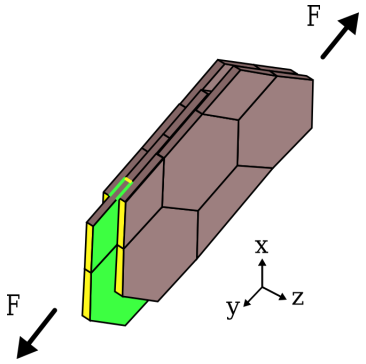

Figure 12: Schematic representation of some platelets lying around the crack surface, with the *basal* and *transverse interfaces* depicted in green and yellow respectively. The black arrows represent the loading direction during bending.

- Transverse interface

Transverse interfaces have a normal collinear with the *y-axis*. Fig. 11-a illustrates the crack surface along with its characteristic dimensions ℓ_c and T_{ci}. The solution of the CC gives the crack initiation surface S_c. In the 3D models we introduce the parameter T_{ci}, which represent the crack dimension along the *z-axis* (see Fig. 11). If $T_{ci} = B$ the crack initiates along the whole sample thickness. On the contrary, $T_{ci} < B$ means the crack initiates only in a fraction of the sample thickness (for instance a single interface between two platelets or the interface between two stacks of platelets).

- Basal interface

  Such interfaces are oriented with their normal collinear with the *z-axis*. Fig. 11-b shows a possible crack shape at initiation following a stress isocontour. The initiation crack front shape can be described only by one parameter, namely the crack surface, S.

3.1.4. 3D micro-scale validation model

The micro-scale sample tested in *along*-configuration is modelled with the same features as the three-dimensional macro-scale model, *e.g.* a minimum mesh size of 0.1 μm and quadratic tetrahedron elements. The mesh contains 30.000 degrees of freedom. A negative displacement is imposed along the *x-axis* on one side of the micro-cantilever on exactly one node (see Fig. 3 - Left). Furthermore, the crack surface location can be varied using the parameter L_i which defines the position of the crack from the base of the cantilever, and the parameter T_i, which defines the position of the interface along the *z-axis*.

3.2. Results

3.2.1. 2D model

Fracture surface observations mainly indicate that crack propagates inside the platelet interface, but also reveal a few broken platelets. The CC enables calculating the force corresponding to crack initiation inside a platelet or at the platelet interface. The crack initiation force assuming that crack initiates inside alumina platelets equals 470 N for a notch tip radius of 5 μm. In the case of crack initiation at the interface, the corresponding crack initiation force determined using the CC in 2D is $F_{init}^{2D} = 60$ N for the same notch tip radius. In the two previously mentioned cases, the crack initiation happens at the notch apex, where the opening stress is maximum. Therefore, crack initiation is more likely to occur at the platelet interface than inside a platelet. However, the

crack initiation force at the interface predicted using the CC underestimates the initiation force measured experimentally (237 ± 24 N), which may be explained by several reasons:

- The notch tip radius ρ_i can have a non-negligible influence on the force at crack initiation. This has been extensively shown in the study of the influence of notch tip radius on stress intensity factor considering a crack perfectly centered with respect to a U-notch [44] [45] [46] [47] [48]. Fig. 13 shows the influence of both the razor-blade notch radius and the crack decentering on the crack initiation force for several configurations. The cyan-star

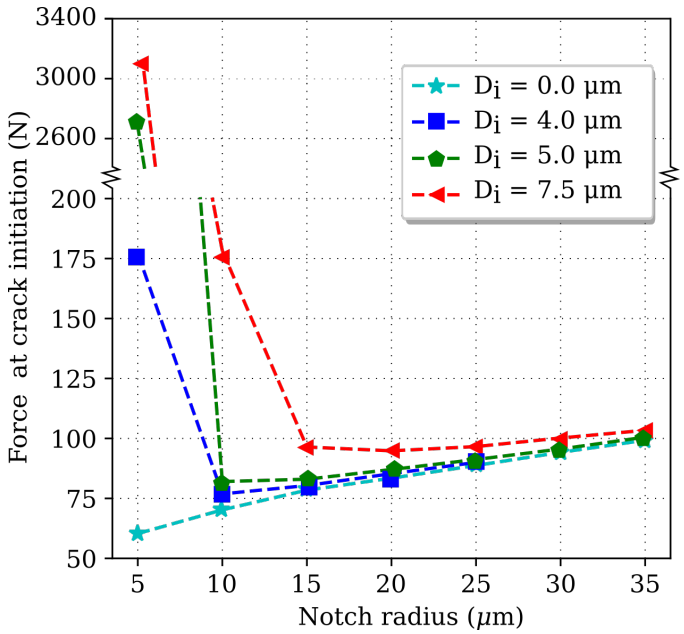

Figure 13: 2D-simulated force at crack initiation as a function of the razor-blade notch radius, for different crack decentering.

curve represents the results for a crack centered relatively to the notch tip, *i.e.* depicting the influence of the notch radius only. The force at failure monotonically increases with increasing notch radius. The force at failure corresponding to a 35 μm notch tip radius remains below 100 N. As the experimental razor-blade notch tip radius range from 5 to 8 μm, the underestimation of the crack initiation force obtained numerically cannot only be explained by uncertainties on the notch tip radius.

- In NLA, since crack initiation occurs at the platelet interface, the crack may possibly be shifted with respect to the notch center as shown on μ-CT slices (see Fig. 6). The blue-

squares, green-pentagons and red-triangles curves in Fig. 13 represent the crack initiation force variation as a function of the notch radius for different crack decentering configurations. It can be seen that the influence of the crack decentering characterized by the parameter D_i (see Fig. 2 - Right) on the crack initiation force remains small for notches with large tip radius - *i.e.* $\rho_i > 20$ μm. When decreasing the notch radius, the influence of the decentering becomes more significant. For a notch tip radius lying in the range of experimentally observed notch tip radii, F_{init}^{2D} matches the experimental values for $D_i \simeq 4.0$ μm. For D_i equals to 7.5 μm the numerical crack initiation force is one order of magnitude higher than the experimental force at crack initiation. Experimentally, the mean of the absolute D_i value across the SENB thickness (along the *z-axis*) equals 7.0 μm. Thus, D_i has a considerable influence, and variates across the sample thickness. This variation cannot be assessed with 2D models.

3.2.2. 3D model

- Crack initiation in transverse interface:

  Fig. 14 shows the displacement to apply to the SENB sample to fulfill the CC as a function of the crack surface for two different values of T_{ci}, the crack initiation thickness. On the left part of the figure, $T_{ci} = 0.5$ μm, which is the thickness of one platelet. On the right part, T_{ci} is equal to 4 μm, equivalent to the thickness of 8 platelets stacked together with no local misalignment within the stack, resulting in a smooth 4 μm long interface.

  For small crack T_{ci}, only the energy part of the CC drives crack initiation since whatever the crack surface, the required imposed displacement to fulfill the energy criterion is larger than the one to fulfill the stress criterion. For larger T_{ci}, the imposed displacement to fulfill the stress criterion is larger (respectively smaller) than the displacement to fulfill the energy criterion for large (small) enough crack surfaces. Therefore, the minimum imposed displacement for which both criteria are fulfilled is attained for the crack surface corresponding to the intersection of both curves. The crack thickness at initiation for which we observe a transition between both cases is equal to 2.5 μm.

  The initiation force as a function of T_{ci} is shown in Fig. 15. The curve can be divided into two distinct parts. For small T_{ci}, the crack initiation force obtained with the 3D model F_{init}^{3D} increases as T_{ci} decreases. When T_{ci} increases from 0.4 μm to 30 μm, F_{init}^{3D} decreases from 230 to 36 N. For T_{ci} ranging from 30 to 1500 μm, no notable variation is noted in the force,

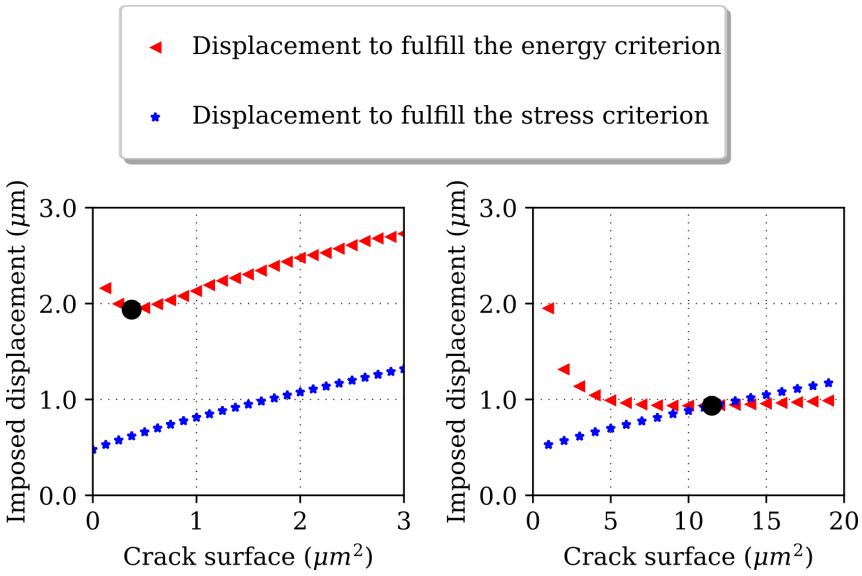

Figure 14: Displacement predicted for T_{ci} equal to (Left) 0.5 μm and (Right) 4.0 μm by each criterion of the CC. The black circle represents the smallest displacement and corresponding crack surface for which both criteria are fulfilled.

reaching a plateau. F_{init}^{2D} value obtained with the 2D model for the same razor-blade notch radius is slightly higher than F_{init}^{3D} in 3D for T_{ci} in the plateau regime. This indicates an overestimation of the 2D model F_{init}^{2D} as compared to the 3D model. This overestimation of F_{init}^{2D} has already been described on scarf adhesive joints [42] and on rhombus hole PMMA specimens under compression [49].

- Crack initiation in basal interface:

  3D FE calculations show that the maximum opening stress at the notch tip σ_{zz} (the opening stress for *basal interfaces*) is 4.4 times lower than σ_{yy} (the opening stress for *transverse interfaces*, see Fig. 12). Fig. 16 - Left shows the distribution of σ_{zz} at mid-sample thickness, corresponding to the *basal interfaces* opening stress distribution around the notch, which decreases with increasing distance from the notch tip.

Provided the incremental energy release rate is an increasing function of the crack area (Fig. 16 - Right), the crack surface can be determined based on the stress iso-contours. It gives a crack initiation force obtained with a 3D model F_{init}^{3D} of 221 N to initiate a *basal interface* crack. This value is similar to the one found earlier for a *transverse interface* with $T_{ci} = 0.4$ μm, and is close to the initiation force measured experimentally (237 $\pm$ 24 N). The initiation crack surface for *basal*

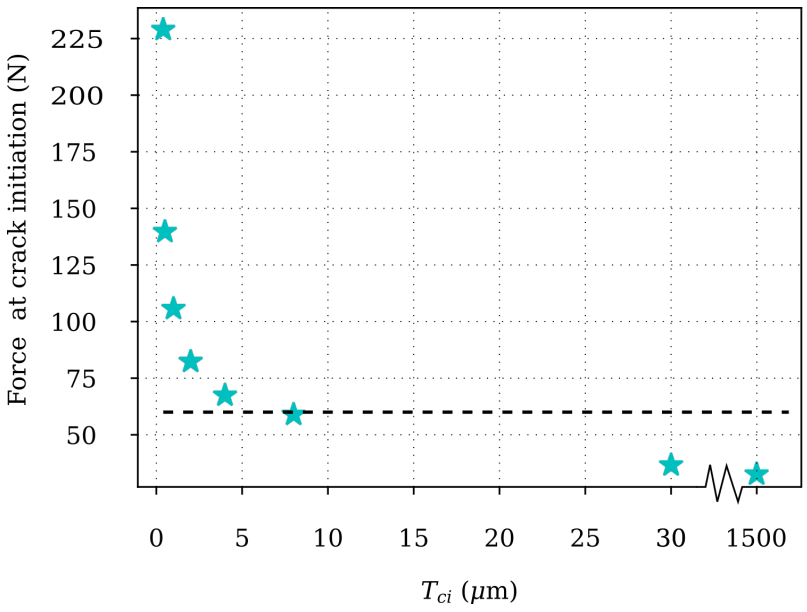

Figure 15: 3D-simulated force at crack initiation for a 4-pts bending sample with $\mathcal{G}_c = 1.9$ J.m^{-2} and $\sigma_c = 438$ MPa. The dashed black line represents the value obtained with a 2-dimensional model.

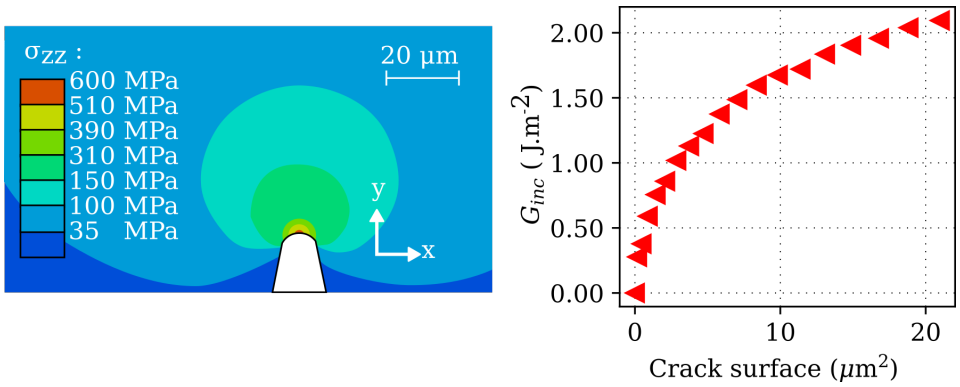

Figure 16: (Left) Macroscopic SENB *basal interface* stress field σ_{zz} around the razor-blade notch at z = B/2. The coordinate system is the same as in Fig. 11. (Right) incremental energy release rate associated with the initiation of a crack in a *basal interface* as a function of the crack surface.

interfaces obtained with the CC is 18.8 μm^2, which corresponds to a 2.8 μm crack extension along the *x-axis* and 7.5 μm crack extension along the *y-axis*.

3.3. Modelling of the micro-cantilever test

Similarly, to the macro-scale, we model two possible configurations for the micro-cantilever test (see Section 2.2.5).

- Crack initiation in *transverse interfaces*

Assuming crack initiation occurs in one *transverse interface* only, F_{init}^{3D} is determined for each possible zone *1*, *2* and *3* as defined in Fig. 3. The values obtained are respectively equals to 1.5, 1.7, 1.6 mN for these three zones, around half of the experimental crack initiation force (3.0 mN). Fig. 17 shows the influence of T_{ci} on F_{init}^{3D} for zone *3* (see Fig. 3). The force obtained increases as T_{ci} decreases. However, the numerical force equals the experimental one for a T_{ci} equals to 0.1 μm, which is inconsistent with the experimental observation (*e.g.* zone *3* has a thickness of 0.49 μm). We can note that for T_{ci} values below 0.75 μm in Fig. 17, energy only has an influence on crack initiation, as could be observed at the macro-scale for small values of T_{ci} (see Fig. 14 - Left).

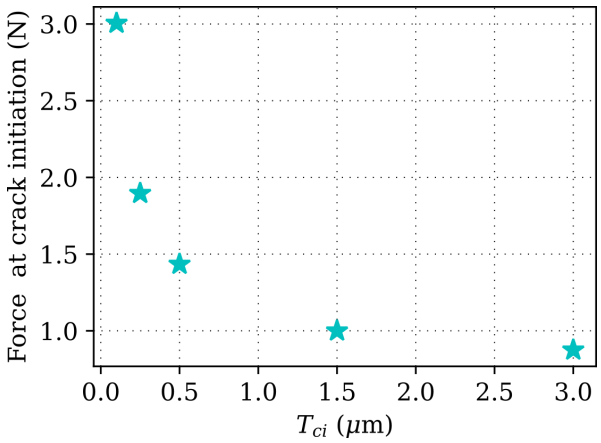

Figure 17: 3D-simulated force at crack initiation in a micro-cantilever beam under bending made of NLA in *along*-configuration.

- Crack initiation in *basal interfaces*

Maximum values for σ_{zz} are obtained in the specimen middle plane perpendicular to the *z-axis* and close to the clamped zone ($y \approx 0$)(see the coordinate system in Fig. 3). Consequently, among all the *basal interfaces* in Fig. 3, *zone 4* depicted in green is the *basal interface* on which σ_{zz} is maximum. Fig. 18 - Left shows the stress field on *zone 4*. In this configuration the CC gives an initiation loading F_{init}^{3D} of $= 9.5$ mN. The comparison of the experimental force (3.0 mN - see Section 2.2.5) to the F_{init}^{3D} computed for the *basal* and *transverse interfaces* shows crack initiation in *transverse interfaces* is more favorable than in *basal interface*. However, both fail to predict accurately crack initiation as none of the crack initiation force values

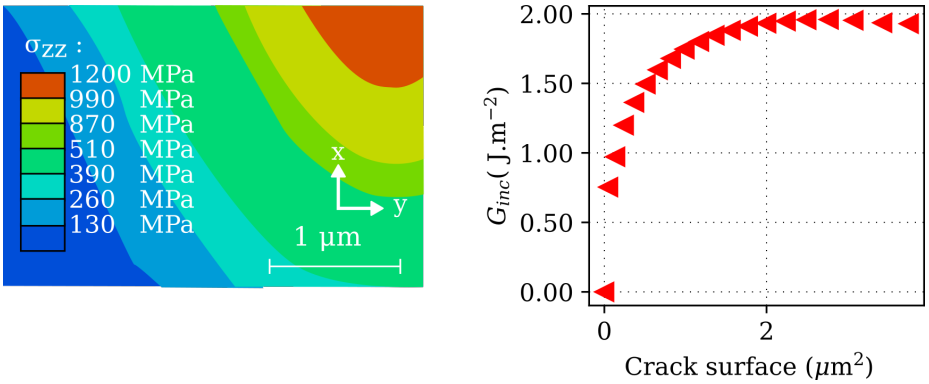

Figure 18: Micro-cantilever *basal interface* on zone *4* (see Fig. 3). (Left) Stress field σ_{zz}. The coordinate system is the same as in Fig. 3. (Right) Incremental energy release rate as a function of the crack surface.

match the experimental force.

4. Discussion

K_{Ic} obtained in nacre-like alumina tested in *along*-configuration is 5.3 ± 0.5 MPa.m$^{0.5}$. This value is similar to the stress intensity factor at initiation in *across*-configuration on similar samples (5.8 ± 0.2 MPa.m$^{0.5}$) [24]. It is larger than the typical critical stress intensity factor of polycrystalline alumina (≈ 3.5 MPa.m$^{0.5}$). These results are listed in Table 3. It shows the efficiency of the brick-and-mortar structure in improving the toughness of NLA in both *across*-configuration and *along*-configuration. In these configurations, critical stress intensity factors at initiation are almost equivalent. However, depending on the platelet orientation, the platelets influence the composite crack initiation differently.

Material	K_{Ic}
NLA - across	5.8 ± 0.2 MPa.m$^{0.5}$
NLA - along	5.3 ± 0.5 MPa.m$^{0.5}$

Table 3: Sum-up of the experimental results obtained for *across*- and *along*-configuration.

The reinforcement mechanism involved in *across*-configuration is based on crack deviation by the microstructure at the macroscale. This deviation leads to a reinforcement for both crack initiation and propagation [25] [35] .

In *along*-configuration, no crack deviation is observed at the macro-scale (Fig. 4). SENB observations at the micro-scale show local crack deviation at the interfaces between platelets, as shown with μ-CT tomography and confocal microscopy. The maximum amplitude of this crack deviation is in the range of tens of micrometers, *i.e.* within the same order of magnitude than the platelet dimensions along the *a* or *b axis* (see Fig. 1). This behavior is further emphasized by the fracture surface observation of micro-cantilever beam tested in bending (Fig. 3). The fracture surface exhibits crenelations resulting from crack deviation by platelets.

The variation of crack decentering across the sample thickness observed experimentally (see Section 2.2.2 and Section 2.2.4) indicates that 3-dimensional effects exist in crack initiation in NLA in *along*-configuration. The load required to initiate a decentered crack has to be higher than for a crack centered with respect to the notch tip as the stress field decreases when moving away from the notch tip in the linear elastic regime.

2D FE models show that the opening stress tens of micrometers away from the notch tip is significantly lower than at the notch tip. Consequently, the numerical crack initiation force obtained by applying the CC on decentered configuration show that this micro-scale crack deviation cannot be neglected. Moreover, 2D models enable accounting only for crack decentering with respect to the notch center. However, the crack tortuosity in *z-direction* is not considered in 2D. Consequently, 3D models must be considered.

CC results from the 3D macroscopic FE models show a competition between two crack opening configurations at the interface between platelets. The results are summarized in Table 4. A crack can initiate from the opening of:

- a *transverse interface* (see Fig. 1-bottom). Relative location of the transverse interface to the notch tip is critical. When the interface is perfectly centered with respect to the notch tip, it is submitted to the largest opening stress. Consequently, if the interface is decentered, the opening stress is lower and crack initiation is less favored. The thinner the interface (*i.e.* the thinner the platelet), the larger the crack initiation force. We found that the *transverse interface* thickness for which the numerical crack initiation force matches the experimental

failure force under 4PB, d_{char}^{init} is equal to 0.4 μm (see Table 4). At such scale, the CC predicts that crack initiation is only driven by energy. Indeed, the applied displacement for which stress criterion is fulfilled is always lower than the displacement to fulfill the energy criterion.

- a *basal interface* (see Fig. 1-bottom). It must be long enough (at least 7.5 μm along the *y-axis*, see Fig. 16) to store enough energy for crack creation. Replacing the platelets in the composite by similar monocrystalline alumina platelets, with the same thickness, but with different dimensions would result in a difference in crack initiation force. This 7.5 μm length is called d_{char}^{init}. It is the characteristic numerical microstructure length for which crack initiation happens. It has to be compared with d_{char}^{exp}, which is the characteristic dimension of the interface, induced by the platelet dimensions (see Table 4). As long as $d_{char}^{exp} > d_{char}^{init}$, the microstructure does not constrain crack initiation. The two quantities being approximately equal means that a change in d_{char}^{exp}, *e.g.* by changing the platelets dimensions, would lead to a change in fracture mechanism.

Scale	Interface type	F_{init}^{exp}	d_{char}^{init} (μm)	d_{char}^{exp} (μm)
macro	transverse	237 $\pm$ 24 N	0.4	0.5
macro	basal	237 $\pm$ 24 N	7.5	10.0
micro	transverse	3 mN	0.1	0.5
micro	basal	3 mN	1.8	10.0

Table 4: Numerical and experimental characteristic lengths for each interface at the micro- and macro-scale, along with the experimental force at failure.

Numerically, we find that crack initiation force for *transverse interface* and *basal interface* are equals when the platelet c dimension (*i.e.* thickness, see Fig. 1-bottom) equals 0.4 μm (providing sufficiently large *basal surface*). Thus, using platelets with larger c dimension, crack should initiate for smaller experimental load, resulting in smaller K_{Ic} and be located on *transverse interface*. On the contrary, decreasing c dimension below 0.4 μm should not have an effect on crack initiation force. In that case, crack initiation will be located on *basal interface*. This clearly emphasized the competition between *basal* and *transverse interfaces* for crack initiation, which primarily depends on the platelet c dimension. It should be noted that the platelet thickness of the SENB samples and micro-cantilever beam is evaluated to approximately 0.5 μm (d_{char}^{exp}, see Table 4), which is closed

to the above-defined optimum thickness. It should be kept in mind that these findings are based on the study of model that does not consider defects or imperfections in the material, *e.g.* platelet misalignment [50]. These imperfections in the microstructure also play a role, thus modifying the extent to which the platelet dimensions play a role in the composite reinforcement.

Both SENB and micro-cantilever beam 3D model emphasize the importance of describing crack initiation using an approach relying on both stress and energy considerations such as the CC. The crack initiation containment reduces strongly the influence of the stress level on crack initiation which ultimately reduces here to an energetic phenomenon. Consequently, it would make the determination of the tensile strength uncertain in an inverse identification procedure, as previously shown by Jimenez and Leguillon [51] and Doitrand *et al.* [41] on micro-samples.

In macroscopic SENB samples, the *z-direction* (*i.e.* along sample thickness) dimension encompass thousands of platelets. Consequently, it is likely that at least one *transverse interface* is well positioned with respect to the notch tip. However, for the micro-cantilever beam, less than 10 platelets are encompassed in the *z-direction*. Consequently, both *basal* and *transverse interfaces* might not be positioned near the beam maximum opening stress zones. This might explain the differences between numerical and experimental crack initiation force for both *basal* and *transverse interfaces*.

5. Conclusion

Crack initiation in NLA has been studied experimentally and numerically on bending samples (SENB samples and micro-cantilever beam) with a platelet orientation, denoted as *along*-configuration, that differs from the literature most-studied configuration [24] [25] [26], denoted as *across*-configuration. NLA exhibits an elastic brittle behavior in *along*-configuration with no stable crack propagation after initiation. The brick-and-mortar microstructure induces a micro-scale interaction with the crack as shown by local crack deviation at the interfaces, but no macroscopic crack deviation from the notch plane. 3D models using the coupled criterion show the crack is contained at initiation at the interface between two platelets. Crack initiation containment leads to a reinforcement of the NLA critical stress intensity factor in *along*-configuration at initiation

when compared to polycrystalline alumina up to values closes to those reported for NLA in *across*-configuration [24].

Acknowledgement

This work was supported by the LABEX MANUTECH-SISE (ANR-10-LABX-0075) of Université de Lyon, within the program "Investissements d'Avenir" (ANR-11-IDEX-0007) operated by the French National Research Agency (ANR).

Moreover, we thank The French Ministry of Education and Research for funding this work, through a PhD scholarship

CRediT

Thomas Duminy: Conceptualization, Methodology, Software, Validation, Investigation, Formal analysis, Writing - Original Draft, Writing - Review & Editing, Visualization, Project administration; **Ronan Henry**: Methodology, Investigation; **Jérôme Adrien**: Investigation, Resources; **Aurélien Doitrand**: Conceptualization, Methodology, Software, Validation, Writing - Review & Editing,Supervision, Project administration, Funding acquisition; **Sylvain Meille**: Conceptualization, Methodology, Validation, Writing - Review & Editing, Supervision, Project administration, Funding acquisition

References

[1] Ritchie, R.O., 2011. The conflicts between strength and toughness. Nature Mater 10, 817–822. https://doi.org/10.1038/nmat311

[2] Evans, A. G. and Heuer, A. H., 1980, Transformation Toughening in Ceramics: Martensitic Transformations in Crack-Tip Stress Fields. Journal of the American Ceramic Society 63, 241–248

[3] Liens, A., Reveron, H., Douillard, T., Blanchard, N., Lughi, V., Sergo, V., Laquai, R., Müller, B.R., Bruno, G., Schomer, S., Fürderer, T., Adolfsson, E., Courtois, N., Swain, M., Chevalier, J., 2020. Phase transformation induces plasticity with negligible damage in ceria-stabilized zirconia-based ceramics. Acta Materialia 183, 261–273. doi:10.1016/j.actamat.2019.10.046

[4] Bower, A.F., Ortiz, M., 1991. A three-dimensional analysis of crack trapping and bridging by tough particles. Journal of the Mechanics and Physics of Solids 39, 815–858. doi:10.1016/0022-5096(91)90026-K

[5] Faber, K.T., Evans, A.G., 1983. Crack deflection processes—I. Theory. Acta Metallurgica 31, 565–576. doi:10.1016/0001-6160(83)90046-9

[6] Melaibari, A., Wagih, A., Basha, M., Kabeel, A.M., Lubineau, G., Eltaher, M.A., 2021. Bio-inspired composite laminate design with improved out-of-plane strength and ductility. Composites Part A: Applied Science and Manufacturing 144, 106362. doi:10.1016/j.compositesa.2021.106362

[7] Sarikaya, M., Aksay, I., 1995. Biomimetic Design and Processing of Materials 11.

[8] Jackson, A., Vincent, J., Turner, R.M., 1988. The Mechanical Design of Nacre. Proceedings of The Royal Society of London. Series B, Biological Sciences (1934-1990) 234, 415–440. doi:10.1098/rspb.1988.0056

[9] Barthelat, F., 2014. Designing nacre-like materials for simultaneous stiffness, strength and toughness: Optimum materials, composition, microstructure and size: Journal of the Mechanics and Physics of Solids, 73, 22-37. Journal of the Mechanics and Physics of Solids 73, 22–37. doi:10.1016/J.JMPS.2014.08.008

[10] Raj, M., Patil, S.P., Markert, B., 2020. Mechanical Properties of Nacre-Like Composites: A Bottom-Up Approach: Journal of Composites Science, 4(2), 35. Journal of Composites Science 4, 35. doi:10.3390/JCS4020035

[11] Meyers, M.A., Chen, P.-Y., Lin, A.Y.-M., Seki, Y., 2008. Biological materials: Structure and mechanical properties. Progress in Materials Science 53, 1–206. doi:10.1016/j.pmatsci.2007.05.002

[12] Espinosa, H.D., Juster, A.L., Latourte, F.J., Loh, O.Y., Gregoire, D., Zavattieri, P.D., 2011. Tablet-level origin of toughening in abalone shells and translation to synthetic composite materials. Nat Commun 2, 173. doi:10.1038/ncomms1172

[13] Barthelat, F., Tang, H., Zavattieri, P., Li, C., Espinosa, H., 2007. On the mechanics of mother-of-pearl: A key feature in the material hierarchical structure. Journal of the Mechanics and Physics of Solids 55, 306–337. doi:10.1016/j.jmps.2006.07.007

[14] Song, F., Soh, A.K., Bai, Y.L., 2003. Structural and mechanical properties of the organic matrix layers of nacre. Biomaterials 24, 3623–3631. doi:10.1016/S0142-9612(03)00215-1

[15] Alghamdi, S., Du, F., Yang, J., Pinder, G., Tan, T., 2020. Tensile and shear behavior of microscale growth layers between nacre in red abalone. Journal of the Mechanics and Physics of Solids 138, 103928. doi:10.1016/j.jmps.2020.103928

[16] Loh, H.-C., Divoux, T., Gludovatz, B., Gilbert, P.U.P.A., Ritchie, R.O., Ulm, F.-J., Masic, A., 2020. Nacre toughening due to cooperative plastic deformation of stacks of co-oriented aragonite platelets. Commun Mater 1, 77. doi:10.1038/s43246-020-00078-y

[17] Bouville, F., Maire, E., Meille, S., Van de Moortèle, B., Stevenson, A.J., Deville, S., 2014. Strong, tough and stiff bioinspired ceramics from brittle constituents. Nature Mater 13, 508–514. doi:10.1038/nmat3915

[18] Pelissari, P.I.B.G.B., Bouville, F., Pandolfelli, V.C., Carnelli, D., Giuliani, F., Luz, A.P., Saiz, E., Studart, A.R., 2018. Nacre-like ceramic refractories for high temperature applications. Journal of the European Ceramic Society 38, 2186–2193. doi:10.1016/j.jeurceramsoc.2017.10.042

[19] Evers, K., Falco, S., Grobert, N., Todd, R.I., 2020. Nacre-like alumina with unique high strain rate capabilities. Journal of the European Ceramic Society 40, 417–426. doi:10.1016/j.jeurceramsoc.2019.09.015

[20] Launey, M.E., Munch, E., Alsem, D.H., Saiz, E., Tomsia, A.P., Ritchie, R.O., 2010. A novel biomimetic approach to the design of high-performance ceramic–metal composites. J R Soc Interface 7, 741–753. doi:10.1098/rsif.2009.0331

[21] Oner Ekiz, O., Dericioglu, A.F., Kakisawa, H., 2009. An efficient hybrid conventional method to fab-

ricate nacre-like bulk nano-laminar composites. Materials Science and Engineering: C 29, 2050–2054. doi:10.1016/j.msec.2009.04.001

[22] Launey, M.E., Munch, E., Alsem, D.H., Barth, H.B., Saiz, E., Tomsia, A.P., Ritchie, R.O., 2009. Designing highly toughened hybrid composites through nature-inspired hierarchical complexity. Acta Materialia 57, 2919–2932. doi:10.1016/j.actamat.2009.03.003

[23] Pelissari, P.I.B.G.B., Pandolfelli, V.C., Carnelli, D., Bouville, F., 2020. Refractory interphase and its role on the mechanical properties of boron containing nacre-like ceramic. Journal of the European Ceramic Society 40, 165–172. doi:10.1016/j.jeurceramsoc.2019.08.034

[24] Saad, H., Radi, K., Douillard, T., Jauffres, D., Martin, C.L., Meille, S., Deville, S., 2020. A simple approach to bulk bioinspired tough ceramics. Materialia 12, 100807. doi:10.1016/j.mtla.2020.100807

[25] Henry, R., Saad, H., Doitrand, A., Deville, S., Meille, S., 2020. Interface failure in nacre-like alumina. Journal of the European Ceramic Society 40, 4694–4699. doi:10.1016/j.jeurceramsoc.2020.05.068

[26] Bouville, F., 2020. Strong and tough nacre-like aluminas: Process–structure–performance relationships and position within the nacre-inspired composite landscape. J. Mater. Res. 35, 1076–1094. doi:10.1557/jmr.2019.418

[27] Le Ferrand, H., Bouville, F., Niebel, T.P., Studart, A.R., 2015. Magnetically assisted slip casting of bioinspired heterogeneous composites. Nature Mater 14, 1172–1179. doi:10.1038/nmat4419

[28] Currey, J. D., 1977. Mechanical properties of mother of pearl in tension. Proceedings of the Royal Society of London. Series B. Biological Sciences, 1125, 443–463. 10.1098/rspb.1977.0050

[29] Akurati, S., Jansson, A., Jones, J.L., Ghosh, D., 2021. Deformation mechanisms in ice-templated alumina–epoxy composites for the different directions of uniaxial compressive loading. Materialia 16, 101054. https://doi.org/10.1016/j.mtla.2021.101054

[30] Chan, X.Y., Chua, C., Tan, S., Le Ferrand, H., 2022. Energy dissipation in composites with hybrid nacre-like helicoidal microstructures. Composites Part B: Engineering 232, 109608. https://doi.org/10.1016/j.compositesb.2021.109608

[31] Abando, N., Saad, H., Monclús, M.A., Deville, S., Molina-Aldareguia, J., Roa, J.J., 2021. Anisotropy effect of bioinspired ceramic/ceramic composites: Can the platelet orientation enhance the mechanical properties at micro- and submicrometric length scale? Journal of the European Ceramic Society 41, 2753–2762. https://doi.org/10.1016/j.jeurceramsoc.2020.12.039

[32] C1421-10, C28 Committee, Test Methods for Determination of Fracture Toughness of Advanced Ceramics at Ambient Temperature. ASTM International. doi:10.1520/C1421-18

[33] Feilden, E., Giovannini, T., Ni, N., Ferraro, C., Saiz, E., Vandeperre, L., Giuliani, F., 2017. Micromechanical strength of individual Al 2 O 3 platelets. Scripta Materialia 131, 55–58. https://doi.org/10.1016/j.scriptamat.2017.01.008

[34] EN ISO 4287 (1998): Geometrical Product Specifications (GPS) — Surface texture:Profile method — Terms, definitions and surface textureparameters, n.d.

[35] Doitrand, A., Henry, R., Saad, H., Deville, S., Meille, S., 2020. Determination of interface fracture properties by micro- and macro-scale experiments in nacre-like alumina. Journal of the Mechanics and Physics of Solids 145, 104143. doi:10.1016/j.jmps.2020.104143

[36] Leguillon, D., 2002. Strength or toughness? A criterion for crack onset at a notch. European Journal of Mechanics - A/Solids 21, 61–72. doi:10.1016/S0997-7538(01)01184-6.

[37] Weißgraeber, P., Hell, S., Becker, W., 2016. Crack nucleation in negative geometries. Engineering Fracture Mechanics 168, 93–104. doi:10.1016/j.engfracmech.2016.02.045

[38] Griffith, A.A., 1921. VI. The phenomena of rupture and flow in solids. Phil. Trans. R. Soc. Lond. A 221, 163–198. doi:10.1098/rsta.1921.0006

[39] Weißgraeber, P., Leguillon, D., Becker, W., 2016. A review of Finite Fracture Mechanics: crack initiation at singular and non-singular stress raisers. Archive of Applied Mechanics 86, 375–401. https://doi.org/10.1007/s00419-015-1091-7

[40] Cornetti, P., Pugno, N., Carpinteri, A., Taylor, D., 2006. Finite fracture mechanics: A coupled stress and energy failure criterion. Engineering Fracture Mechanics 73, 2021–2033. https://doi.org/10.1016/j.engfracmech.2006.03.010

[41] Doitrand, A., Henry, R., Chevalier, J., Meille, S., 2020. Revisiting the strength of micron-scale ceramic platelets. Journal of the American Ceramic Society 103. doi:10.1111/jace.17148

[42] Doitrand, A., Leguillon, D., 2018. Comparison between 2D and 3D applications of the coupled criterion to crack initiation prediction in scarf adhesive joints. International Journal of Adhesion and Adhesives 85, 69–76. doi:10.1016/j.ijadhadh.2018.05.022

[43] Doitrand, A., Leguillon, D., 2018. 3D application of the coupled criterion to crack initiation prediction in epoxy/aluminum specimens under four point bending. International Journal of Solids and Structures 143, 175–182. doi:10.1016/j.ijsolstr.2018.03.005

[44] Damani, R., Gstrein, R., Danzer, R., 1996. Critical notch-root radius effect in SENB-S fracture toughness testing. Journal of the European Ceramic Society 16, 695–702. doi:10.1016/0955-2219(95)00197-2

[45] Fett, T., 2005. Influence of a finite notch root radius on fracture toughness. Journal of the European Ceramic Society 25, 543–547. doi:10.1016/j.jeurceramsoc.2004.01.010

[46] Picard, D., Leguillon, D., Putot, C., 2006. A method to estimate the influence of the notch-root radius on the fracture toughness measurement of ceramics. Journal of the European Ceramic Society 26, 1421–1427. doi:10.1016/j.jeurceramsoc.2005.02.016

[47] Leguillon, D., Yosibash, Z., 2003. Crack onset at a V-notch. Influence of the notch tip radius. International Journal of Fracture 122, 1–21. https://doi.org/10.1023/B:FRAC.0000005372.68959.1d

[48] Carpinteri, A., Cornetti, P., Sapora, A., 2012. A Finite Fracture Mechanics approach to the asymptotic behaviour of U-notched structures. Fatigue and Fracture of Engineering Materials and Structures 35, 451–457. https://doi.org/10.1111/j.1460-2695.2011.01637.x

[49] Doitrand, A., Estevez, R., Leguillon, D., 2019. Experimental characterization and numerical modeling of crack initiation in rhombus hole PMMA specimens under compression. European Journal of Mechanics - A/Solids 76, 290–299. doi:10.1016/j.euromechsol.2019.04.013

[50] Saad, H., Douillard, T., Malchère, A., Steyer, P., Meille, S., Deville, S., Reynard, B., 2022. Toughening mechanisms in nacre-like alumina revealed by in-situ imaging of stress. Journal of the European Ceramic Society 42, 6757–6761. https://doi.org/10.1016/j.jeurceramsoc.2022.07.040

[51] Jiménez Alfaro, S., Leguillon, D., 2021. Finite Fracture Mechanics at the micro-scale. Application to bending tests of micro cantilever beams. Engineering Fracture Mechanics 108012. doi:10.1016/j.engfracmech.2021.108012